B.1 Introduction

By 2060, over one third of the Europeans will be above 65 years old according to the study reported by the European Commission in 2015 [1]. According to this study, the ratio between the retired seniors and the working people will be doubled. This will result in an increased demand for in-home activity recognition systems for elder people to distinguish falls from other normal activities such as, walking, sitting, standing, and jumping. These activities follow three-dimensional (3D) trajectories. This motivates us to analyze the influence of human activities on the Doppler power spectrum of 3D fixed-to-fixed (F2F) indoor channels.

The aim of this paper is to design a channel simulator that helps to analyze the influence of fall activities of the people on the approximated Doppler power spectrum characteristics of 3D indoor channels. In the literature, many fall detection systems have been developed using video-surveillance [2, 3] or wearable sensors [4]. The main disadvantage of video surveillance-based or portable sensor-based fall detection systems is that the person might be outside the surveillance area or forget to wear the sensor. The authors of [5, 6] tracked the motion of people by analyzing the measured received signal power. In this paper, we analyze the approximation of the true Doppler power spectrum of indoor channels, which is influenced by the movement of people, by means of the spectrogram.

In the literature, the Doppler frequency caused by the motion of the scatterers has been incorporated in wide-sense stationary vehicle-to-vehicle [7], F2F [8], and fixed-to-mobile channels [9]. The time-variant (TV) Doppler effect caused by moving scatterers has been modelled in two-dimensional (2D) indoor F2F channels in [10]. In this paper, we use the spectrogram to study the influence of human activities, such as walking and falling, on the characteristics of 3D indoor multipath propagation channels. The spectrogram is one of the time-frequency representations used to represent the TV power spectrum of multi-component signals [11]. It has many applications in the area of TV signals [12], speech analysis and identification [13], acoustics [14], and seismology [15]. Furthermore, it has first been introduced in non-stationary multipath fading channels with variations of the mobile speed in [16]. One of the main disadvantages of the spectrogram, is the cross-term that reduces its resolution. Due to this problem, contributions to enhance the resolution of the spectrogram in mobile fading channels can be found in [10, 16, 17].

This paper begins with the introduction of a new 3D non-stationary single-input single-output (SISO) F2F channel model with TV parameters, such as the elevation angles of departure (EAODs), azimuth angles of departure (AAODs), elevation angles of arrival (EAOAs), azimuth angles of arrival (AAOAs), vertical angles of motion (VAOMs), and horizontal angles of motion (HAOMs) of the moving scatterers. The model also accounts for the TV speed of the moving scatterers. From these TV parameters, the expressions of the TV Doppler frequencies, instantaneous channel phases, and complex channel gain of the multipath non-stationary F2F channels are provided. Furthermore, an approximation of the

spectrogram of the complex channel gain is presented in closed-form as a sum of two terms, an auto-term and a cross-term. The auto-term provides an insight into the approximation of the desired Doppler power spectrum of the proposed model. On the other hand, the cross-term, which is considered as an undesired spectral interference term, reduces the resolution of the spectrogram. The closed-form approximation of the spectrogram is confirmed by simulations.

The rest of the paper is organized as follows. Section B.2 illustrates the 3D multipath propagation F2F propagation scenario with moving and fixed scatterers. Section B.3 discusses the TV channel parameters, TV Doppler frequencies, and the complex channel gain of our proposed model. Section B.4 provides the closed-form approximation of the spectrogram including the auto-term and the cross-term of the complex channel gain. Section B.5 discusses the numerical results of the spectrogram and illustrates the influence of human activities on 3D indoor multipath channels. Section B.6 summarizes our contribution and proposes possible extensions of our work.

B.2 The 3D Multipath Propagation Scenario

We consider the 3D indoor multipath propagation scenario presented in Fig. B.1, which consists of a fixed transmitter (T_x), a fixed receiver (R_x), fixed objects, and moving persons. A more abstract representation of such a 3D indoor propagation scenario leads to the geometrical channel model shown in Fig. B.2. This geometrical model describes a propagation scenario with a fixed transmitter (T_x) at position $\left(x^T, y^T, z^T\right)$ and a fixed receiver (R_x) located at $\left(x^R, y^R, z^R\right)$. The scenario includes N moving persons, modelled for simplicity by N moving point scatterers S_n^{M} (▲) for $n = 1, 2, \ldots, N$, where each one starts from an initial position at $\left(x_n^{\mathrm{M}}, y_n^{\mathrm{M}}, z_n^{\mathrm{M}}\right)$ and moves with a TV velocity vector $\vec{v}_n(t)$. The 3D trajectory of each moving scatterer S_n^{M} is described by its TV speed $v_n(t) = |\vec{v}_n(t)|$, the TV VAOM $\beta_{v_n}(t)$, and the TV HAOM $\alpha_{v_n}(t)$. In addition, the scenario includes walls and other objects which are modelled for simplicity as M fixed point scatterers S_m^{F} (★) for $m = 1, 2, \ldots, M$. Furthermore, single bounce scattering is assumed, i.e., each plane wave that the transmitter emits bounces on either a fixed or moving scatterer before arriving at the receiver. Both T_x and R_x are equipped with omnidirectional antennas. It is also assumed that the line-of-sight (LOS) is obstructed. The parameters $\beta_n^T(t)$, $\alpha_n^T(t)$, $\beta_n^R(t)$, and $\alpha_n^R(t)$ shown in Fig. B.2 are TV functions that denote EAOD, AAOD, EAOA, and AAOA, respectively.

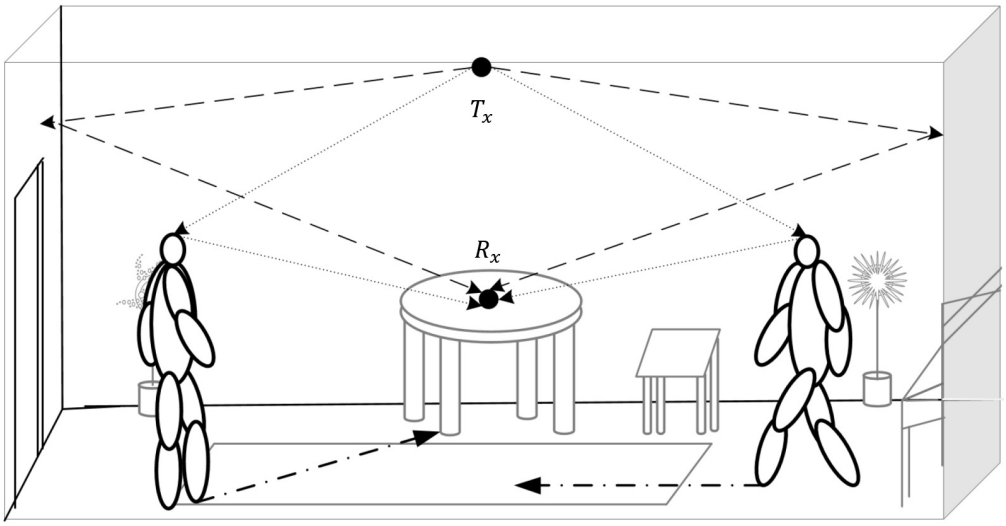

Figure B.1: A 3D non-stationary indoor multipath propagation scenario with moving persons.

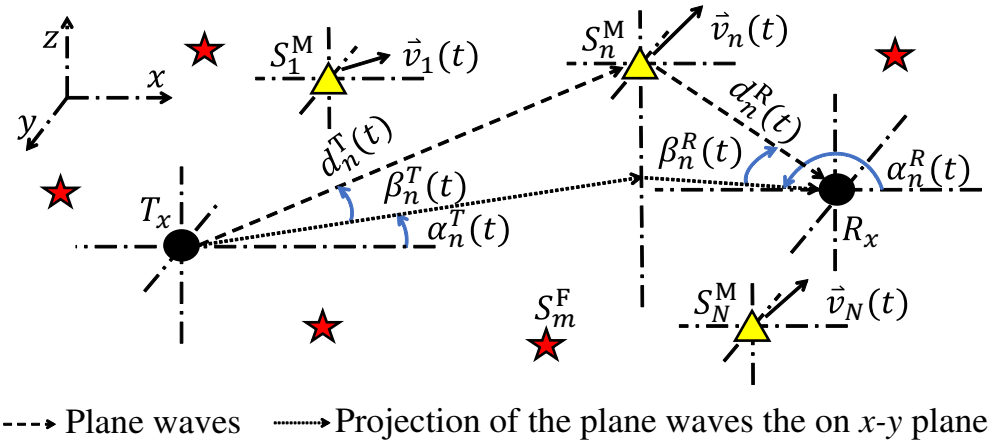

Figure B.2: A 3D non-stationary indoor multipath propagation scenario with N moving scatterers S_n^{M} $(n = 1, 2, \ldots, N)$ and M fixed scatterers S_m^{F} $(m = 1, 2, \ldots, M)$.

B.3 Derivation of the Complex Channel Gain

B.3.1 TV Velocity and TV Angular Functions

According to Fig. B.2, each moving scatterer S_n^{M} is described by a TV velocity vector $\vec{v}_n(t)$ which is given by

$$\vec{v}_n(t) = \left[v_{n,x}(t) \;,\; v_{n,y}(t) \;,\; v_{n,z}(t)\right] \tag{B.1}$$

where the velocities $v_{n,x}(t)$, $v_{n,y}(t)$, and $v_{n,z}(t)$ can be expressed in terms of the TV speed $v_n(t)$, TV VAOM $\beta_{v_n}(t)$, and TV HAOM $\alpha_{v_n}(t)$ as

$$v_{n,x}(t) = v_n(t)\cos(\beta_{v_n}(t))\cos(\alpha_{v_n}(t)) \tag{B.2}$$

$$v_{n,y}(t) = v_n(t)\cos(\beta_{v_n}(t))\sin(\alpha_{v_n}(t)) \tag{B.3}$$

$$v_{n,z}(t) = v_n(t)\sin(\beta_{v_n}(t)). \tag{B.4}$$

The TV locations $x_n(t)$, $y_n(t)$, and $z_n(t)$ of the nth moving scatterer S_n^{M} can be obtained from each component of the TV velocity vector $\vec{v}_n(t)$ by

$$x_n(t) = x_n^{\mathrm{M}} + \int_0^t v_{n,x}(t')dt' \tag{B.5}$$

$$y_n(t) = y_n^{\mathrm{M}} + \int_0^t v_{n,y}(t')dt' \tag{B.6}$$

$$z_n(t) = z_n^{\mathrm{M}} + \int_0^t v_{n,z}(t')dt'. \tag{B.7}$$

From the TV locations in (B.5)–(B.7), the TV Euclidean distance $d_n^T(t)$ between T_x and the nth moving scatterer S_n^{M} can be obtained as

$$d_n^T(t) = \sqrt{(x_n(t)-x^T)^2 + (y_n(t)-y^T)^2 + (z_n(t)-z^T)^2}. \tag{B.8}$$

Similarly, the TV Euclidean distance $d_n^R(t)$ between R_x and the nth moving scatterer S_n^{M} is given by

$$d_n^R(t) = \sqrt{(x_n(t)-x^R)^2 + (y_n(t)-y^R)^2 + (z_n(t)-z^R)^2}. \tag{B.9}$$

From the TV locations in (B.5)–(B.7) and the TV distances in (B.8) and (B.9), one can obtain the TV EAOD $\beta_n^T(t)$, TV AAOD $\alpha_n^T(t)$, TV EAOA $\beta_n^R(t)$, and TV AAOA $\alpha_n^R(t)$ as follows:

$$\beta_n^T(t) = \arcsin\left(\frac{z_n(t)-z^T}{d_n^T(t)}\right) \tag{B.10}$$

$$\alpha_n^T(t) = \mathrm{atan2}\left(y_n(t)-y^T,\, x_n(t)-x^T\right) \tag{B.11}$$

$$\beta_n^R(t) = \arcsin\left(\frac{z_n(t)-z^R}{d_n^R(t)}\right) \tag{B.12}$$

$$\alpha_n^R(t) = \mathrm{atan2}\left(y_n(t)-y^R,\, x_n(t)-x^R\right). \tag{B.13}$$

The atan2 function in (B.11) stands for the inverse trigonometric function that returns the angle between $-\pi$ and π, unlike the arctan function which returns the angle between $-\pi/2$

and $\pi/2$. It should be mentioned that the elevation angles $\beta_n^T(t)$ and $\beta_n^R(t)$ range from $-\pi/2$ to $\pi/2$ and the azimuth angles $\alpha_n^T(t)$ and $\alpha_n^R(t)$ from $-\pi$ and π. The TV HAOM $\alpha_{v_n}(t)$ and TV VAOM $\beta_{v_n}(t)$ can be expressed by the instantaneous velocities $v_{n,x}(t)$, $v_{n,y}(t)$, and $v_{n,z}(t)$ of the nth moving scatterer by

$$\alpha_{v_n}(t) = \operatorname{atan2}\left(v_{n,y}(t), v_{n,x}(t)\right) \tag{B.14}$$

$$\beta_{v_n}(t) = \arcsin\left(\frac{v_{n,z}(t)}{\sqrt{v_{n,x}^2(t) + v_{n,y}^2(t) + v_{n,z}^2(t)}}\right) \tag{B.15}$$

respectively, where $\alpha_{v_n}(t) \in (-\pi, \pi]$ and $\beta_{v_n}(t) \in \left[-\frac{\pi}{2}, \frac{\pi}{2}\right]$.

The unit vector of departure $\vec{\phi}_n^T(t)$ of the wave transmitted from T_x towards the nth moving scatterer S_n^{M} can be expressed by the TV EAOD $\beta_n^T(t)$ and AAOD $\alpha_n^T(t)$ as follows

$$\vec{\phi}_n^T(t) = \begin{bmatrix} \cos\left(\alpha_n^T(t)\right)\cos\left(\beta_n^T(t)\right) \\ \sin\left(\alpha_n^T(t)\right)\cos\left(\beta_n^T(t)\right) \\ \sin\left(\beta_n^T(t)\right) \end{bmatrix}. \tag{B.16}$$

Analogously, the unit vector of arrival $\vec{\phi}_n^R(t)$ of the wave travelling from the nth moving scatterer S_n^{M} to R_x can be expressed by the TV EAOA $\beta_n^R(t)$ and AAOA $\alpha_n^R(t)$ as follows

$$\vec{\phi}_n^R(t) = \begin{bmatrix} \cos\left(\alpha_n^R(t)\right)\cos\left(\beta_n^R(t)\right) \\ \sin\left(\alpha_n^R(t)\right)\cos\left(\beta_n^R(t)\right) \\ \sin\left(\beta_n^R(t)\right) \end{bmatrix}. \tag{B.17}$$

B.3.2 Modelling the TV Doppler Frequency

The Doppler frequency $f_n(t)$ caused by the motion of the nth moving scatterer S_n^{M} can be calculated by

$$\begin{aligned} f_n(t) &= -\frac{\vec{v}_n(t)\,\vec{\phi}_n^T(t) + \vec{v}_n(t)\,\vec{\phi}_n^R(t)}{\lambda} \\ &= -f_{n,\max}(t) \\ &\times \Bigg\{ \cos\left(\beta_{v_n}(t)\right)\left[\cos\left(\beta_n^T(t)\right)\cos\left(\alpha_n^T(t) - \alpha_{v_n}(t)\right)\right. \\ &+ \left.\cos\left(\beta_n^R(t)\right)\cos\left(\alpha_{v_n}(t) - \alpha_n^R(t)\right)\right] + \sin\left(\beta_{v_n}(t)\right) \\ &\times \left[\sin\left(\beta_n^T(t)\right) + \sin\left(\beta_n^R(t)\right)\right] \Bigg\} \end{aligned} \tag{B.18}$$

where

$$f_{n,\max}(t) = \frac{v_n(t)}{\lambda} \tag{B.19}$$

denotes the maximum Doppler frequency. The symbol λ in (B.19) represents the wavelength of the carrier signal. The Doppler frequency $f_n(t)$ in (B.18) is a TV deterministic process if the initial position $\left(x_n^{\mathrm{M}},\, y_n^{\mathrm{M}},\, z_n^{\mathrm{M}}\right)$ and the velocity $\vec{v}_n(t)$ of the scatterer S_n^{M} are known and the locations of T_x and R_x are fixed.
The model for the Doppler frequencies $f_n(t)$ in (B.18) includes several special cases. For example, if the function $\beta_{v_n}(t)$ equals zero, then (B.18) reduces to

$$\begin{aligned} f_n(t) = &- f_{n,\max}(t)\Big\{ \cos\left(\beta_n^T(t)\right)\, \cos\left(\alpha_n^T(t) - \alpha_{v_n}(t)\right) \\ &+ \cos\left(\beta_n^R(t)\right)\, \cos\left(\alpha_{v_n}(t) - \alpha_n^R(t)\right)\Big\} \end{aligned} \tag{B.20}$$

which is analogous to the Doppler frequencies of moving scatterers in 3D non-stationary vehicle-to-vehicle (V2V) channels. If we set the functions $\beta_{v_n}(t)$, $\beta_n^T(t)$, and $\beta_n^R(t)$ to zero, and $\alpha_{v_n}(t)$ is supposed to be a constant, i.e., $\alpha_{v_n}(t) = \alpha_{v_n}$, then (B.18) reduces further to

$$\begin{aligned} f_n(t) = &- f_{n,\max}(t)\Big\{ \cos\left(\alpha_n^T(t) - \alpha_{v_n}\right) \\ &+ \cos\left(\alpha_{v_n} - \alpha_n^R(t)\right)\Big\} \end{aligned} \tag{B.21}$$

which equals the Doppler frequency caused by a moving scatterer in 2D non-stationary F2F channels as modelled in [10]. Moreover, if all the parameters in (B.18) are constants, then the Doppler frequency becomes independent of time, i.e.,

$$\begin{aligned} f_n = &- f_{n,\max}\Big\{ \cos\left(\beta_{v_n}\right)\left[\cos\left(\beta_n^T\right)\cos\left(\alpha_n^T - \alpha_{v_n}\right)\right. \\ &\left. + \cos\left(\beta_n^R\right)\cos\left(\alpha_{v_n} - \alpha_n^R\right)\right] + \sin\left(\beta_{v_n}\right) \\ &\times \left[\sin\left(\beta_n^T\right) + \sin\left(\beta_n^R\right)\right]\Big\} \end{aligned} \tag{B.22}$$

which equals the Doppler frequency of 3D stationary F2F channels with scatterers moving with constant velocities and time-invariant angular parameters. Finally, if we set β_{v_n} to zero, then the expression in (B.22) reduces to

$$\begin{aligned} f_n \;\; = \;\; -f_{n,\max}\Big\{ &\cos\left(\beta_{v_n}\right)\left[\cos\left(\beta_n^T\right)\cos\left(\alpha_n^T - \alpha_{v_n}\right)\right. \\ &\left. + \cos\left(\beta_n^R\right)\cos\left(\alpha_{v_n} - \alpha_n^R\right)\right]\Big\} \end{aligned} \tag{B.23}$$

which equals the expression of the Doppler frequencies of scatterers moving in the x-y plane of 2D wide-sense stationary channels.

For the purpose of this paper, we approximate the Doppler frequencies $f_n(t)$ in (B.18) by L piecewise linear functions according to

$$f_n(t) \approx f_{n,l}(t) = f_n(t_l) + k_{n,l}(t - t_l) \tag{B.24}$$

for $t_l < t \leq t_{l+1}$ and $l = 0, 1, \ldots, L$, where

$$k_{n,l} = \frac{f_n(t_{l+1}) - f_n(t_l)}{t_{l+1} - t_l}. \tag{B.25}$$

It should be noted that the difference between two adjacent time instances t_{l+1} and t_l, i.e., $\Delta = t_{l+1} - t_l$, is the same for all values of $l = 0, 1, \ldots, L$.

B.3.3 Modelling the TV Channel Phases and Complex Channel Gains

As shown in [18], the instantaneous channel phases $\theta_{n,\mathrm{M}}(t)$ of the multipath component associated with the nth moving scatterer S_n^{M} can be computed from the Doppler frequency $f_n(t)$ by

$$\theta_{n,\mathrm{M}}(t) = 2\pi \int_{-\infty}^{t} f_n(t')dt' = \theta_{n,\mathrm{M}} + 2\pi \int_{0}^{t} f_n(t')dt' \tag{B.26}$$

where the first term $\theta_{n,\mathrm{M}}$ denotes the initial channel phase at $t = 0$ which is generally unknown and will thus be modelled by a random variable with a uniform distribution between 0 and 2π, i.e., $\theta_{n,\mathrm{M}} \sim \mathcal{U}(0, 2\pi]$. After the instantaneous channel phases $\theta_{n,\mathrm{M}}(t)$ are obtained, the complex channel gain $\mu(t)$ of the $N + M$ received multipath components can be modelled by

$$\mu(t) = \sum_{n=1}^{N} c_{n,\mathrm{M}}\, e^{j\theta_{n,\mathrm{M}}(t)} + \sum_{m=1}^{M} c_{m,\mathrm{F}}\, e^{j\theta_{m,\mathrm{F}}}. \tag{B.27}$$

The first term in (B.27) represents the sum of the multipath components associated with the N moving scatterers. Each component is determined by a stochastic phase process $\theta_{n,\mathrm{M}}(t)$ and a constant path gain $c_{n,\mathrm{M}}$. The second term in (B.27) represents the sum of the multipath components associated with the M fixed scatterers. The parameters $c_{n,\mathrm{M}}$ and $\theta_{n,\mathrm{M}}$ ($c_{m,\mathrm{F}}$ and $\theta_{m,\mathrm{F}}$) are the path gain and the phase shift caused by the interaction of the signal with the nth moving (mth fixed) scatterer S_n^{M} (S_m^{F}), respectively. It has to be mentioned that $\theta_{n,\mathrm{M}}$ and $\theta_{m,\mathrm{F}}$ are uniformally, independent, and identically distributed in the interval $(0, 2\pi]$. The expression in (B.27) represents a stochastic model for the complex channel gain of a 3D non-stationary indoor F2F channel with moving and fixed scatterers.

From this model, the TV mean Doppler shift $B_f^{(1)}(t)$ and the TV Doppler spread $B_f^{(2)}(t)$ can be calculated by [18]

$$B_f^{(1)}(t) = \frac{\sum\limits_{n=1}^{N} c_{n,\mathrm{M}}^2 \, f_n(t)}{\sum\limits_{n=1}^{N} c_{n,\mathrm{M}}^2 + \sum\limits_{m=1}^{M} c_{m,\mathrm{F}}^2} \tag{B.28}$$

and

$$B_f^{(2)}(t) = \sqrt{\frac{\sum\limits_{n=1}^{N} c_{n,\mathrm{M}}^2 \, f_n^2(t)}{\sum\limits_{n=1}^{N} c_{n,\mathrm{M}}^2 + \sum\limits_{m=1}^{M} c_{m,\mathrm{F}}^2} - \left(B_f^{(1)}(t)\right)^2} \tag{B.29}$$

respectively.

B.4 Spectrogram Analysis

The spectrogram $S_\mu(f,t)$ of $\mu\,(t)$ is obtained in 3 steps. In the first step, the TV complex channel gain $\mu(t)$ is multiplied by a window function $h(t)$. Here, the chosen window function is a Gaussian function

$$h(t) = \frac{1}{\sqrt{\sigma_w \sqrt{\pi}}} e^{-\frac{t^2}{2\sigma_w^2}} \tag{B.30}$$

where σ_w is the Gaussian window spread parameter. In general, the window function is real and even with unit energy, i.e., $\int_\infty^\infty h^2(t)dt = 1$. The short-time complex channel gain $x(\tau,t)$ is defined in [19, Eq. (2.3.1)] by

$$x(\tau,t) = \mu(\tau)h(\tau - t) \tag{B.31}$$

where τ denotes the running time, and t is the local time. The second step is to compute the Fourier transform of the short-time signal w.r.t. the running time τ to obtain the short-time Fourier transform (STFT). The STFT $X(f,t)$ of the complex channel gain $\mu(t)$ in (B.27) can be obtained as

$$\begin{aligned} X(f,t) &= \int_{-\infty}^{\infty} x(\tau,t) e^{-j2\pi f\tau} d\tau \\ &= \frac{e^{-j2\pi ft}}{\sqrt{\sigma_w}\pi^{1/4}} \Bigg\{ \sum_{n=1}^{N} \mu_{n,\mathrm{M}}(t) \, G\left(f, f_{n,l}(t), \sigma_{x,n,l,\mathrm{M}}^2\right) \\ &\quad + \sum_{m=1}^{M} \mu_{m,\mathrm{F}} \, G\left(f, 0, \sigma_{x,m,\mathrm{F}}^2\right) \Bigg\} \end{aligned} \tag{B.32}$$

for $t_l < t \leq t_{l+1}$ $(l = 0, 1, \cdots, L)$, where

$$G\left(f, f_{n,l}(t), \sigma^2_{x,n,l,\mathrm{M}}\right) = \frac{e^{-\frac{(f-f_{n,l}(t))^2}{2\sigma^2_{x,n,l,\mathrm{M}}}}}{\sqrt{2\pi}\sigma_{x,n,l,\mathrm{M}}} \tag{B.33}$$

$$\sigma^2_{x,n,l,\mathrm{M}} = \frac{1 - j2\pi\sigma_w^2 k_{n,l}}{(2\pi\sigma_w)^2} \tag{B.34}$$

$$\sigma^2_{x,m,\mathrm{F}} = \frac{1}{(2\pi\sigma_w)^2}. \tag{B.35}$$

The function $\mu_{n,\mathrm{M}}(t)$ (parameter $\mu_{m,\mathrm{F}}$) denotes the complex gain corresponding to the nth moving (mth fixed) scatterer S_n^{M} (S_m^{F}). The expression in (B.33) represents a complex Gaussian function with a time-variant mean $f_{n,l}(t)$ and variance $\sigma^2_{x,n,l,\mathrm{M}}$. The parameter $k_{n,l}$ in (B.34), which is defined in (B.25), denotes the rate of change of the Doppler frequency $f_{n,l}(t)$. By multiplying the STFT $X(f,t)$ presented in (B.32) by its complex conjugate, one obtains the spectrogram $S_\mu(f,t)$ as follows

$$S_\mu(f,t) = |X(f,t)|^2 = S_\mu^{(a)}(f,t) + S_\mu^{(c)}(f,t) \tag{B.36}$$

where $S_\mu^{(a)}(f,t)$ and $S_\mu^{(c)}(f,t)$ denote the *auto-term* and the *cross-term*, respectively. The auto-term is given by

$$\begin{aligned} S_\mu^{(a)}(f,t) = &\sum_{n=1}^{N} c^2_{n,\mathrm{M}}\, G\left(f, f_{n,l}(t), \sigma^2_{n,l,\mathrm{M}}\right) \\ &+ \sum_{m=1}^{M} c^2_{m,\mathrm{F}}\, G\left(f, 0, \sigma^2_{m,\mathrm{F}}\right) \end{aligned} \tag{B.37}$$

for $t_l < t \leq t_{l+1}$, where

$$\sigma^2_{n,l,\mathrm{M}} = \frac{1 + \left(2\pi\sigma_w^2 k_{n,l}\right)^2}{2(2\pi\sigma_w)^2} \tag{B.38}$$

$$\sigma^2_{m,\mathrm{F}} = \frac{1}{2(2\pi\sigma_w)^2}. \tag{B.39}$$

The auto-term $S_\mu^{(a)}(f,t)$ given by (B.37) is real and positive. This term consists of a sum of $N + M$ components and represents the approximation of the desired Doppler power characteristics of the 3D indoor non-stationary F2F channel with moving scatterers. It is a sum of weighted Gaussian functions, where the weighting factors are given by the squared path gains $c^2_{n,\mathrm{M}}$ and $c^2_{m,\mathrm{F}}$ of the moving scatterers and the fixed scatterers, respectively. The Gaussian functions of the first term in (B.37) are centered on $f_{n,l}(t)$ of the moving scatterers. The second term of $S_\mu^{(a)}(f,t)$ in (B.37) is centered on the origin as the fixed scatterers do

not cause Doppler shifts in F2F channels. The cross-term $S_\mu^{(c)}(f,t)$, which is given by (B.40) at the bottom of this page, represents the undesired spectral interference term consisting of $(N+M)\,(N+M-1)/2$ components. This term is a real, but not necessarily a positive function. The operator $\Re\{\cdot\}$ in (B.40) denotes the real part of a complex function. It is obvious that the auto-term $S_\mu^{(a)}(f,t)$ in (B.37) is independent of the phases $\theta_{n,\mathrm{M}}$ and $\theta_{m,\mathrm{F}}$, unlike the cross-term $S_\mu^{(c)}(f,t)$ in (B.40) which depends on them. Hence, the cross-term can be eliminated by applying the expectation operator to the spectrogram $S_\mu(f,t)$ and averaging over the random channel phases $\theta_{n,\mathrm{M}}$ and $\theta_{m,\mathrm{F}}$, i.e., $E\left\{S_\mu(f,t)\right\}\big|_{\theta_{n,\mathrm{M}},\theta_{m,\mathrm{F}}} = S_\mu^{(a)}(f,t)$.

The TV mean Doppler shift $B_\mu^{(1)}(t)$ and the TV Doppler spread $B_\mu^{(2)}(t)$ can be computed from the spectrogram $S_\mu(f,t)$ by [10]

$$B_\mu^{(1)}(t) = \frac{\int\limits_{-\infty}^{\infty} f S_\mu(f,t)df}{\int\limits_{-\infty}^{\infty} S_\mu(f,t)df} \tag{B.41}$$

and

$$B_\mu^{(2)}(t) = \sqrt{\frac{\int\limits_{-\infty}^{\infty} f^2 S_\mu(f,t)df}{\int\limits_{-\infty}^{\infty} S_\mu(f,t)df} - \left(B_\mu^{(1)}(t)\right)^2} \tag{B.42}$$

respectively.

B.5 Numerical Results

In this section, numerical results are presented for a 3D non-stationary indoor scenario, which is illustrated in Fig. B.3. The value of the carrier frequency f_0 was chosen to be 5.9 GHz. The

---

$$\begin{aligned} S_\mu^{(c)}(f,t) = \\ \frac{2}{\sigma_w\sqrt{\pi}}\Bigg[&\sum_{n=1}^{N-1}\sum_{m=n+1}^{N} \Re\Big\{ G\left(f, f_{n,l}(t), \sigma^2_{x,n,l,\mathrm{M}}\right)\, G^*\left(f, f_{m,l}(t), \sigma^2_{x,m,l,\mathrm{M}}\right)\, \mu_{n,\mathrm{M}}(t)\, \mu^*_{m,\mathrm{M}}(t) \Big\} \\ &+ \sum_{n=1}^{M-1}\sum_{m=n+1}^{M} \Re\Big\{ G\left(f, 0, \sigma^2_{x,n,\mathrm{F}}\right)\, G^*\left(f, 0, \sigma^2_{x,m,\mathrm{F}}\right)\, \mu_{n,\mathrm{F}}\, \mu^*_{m,\mathrm{F}} \Big\} \\ &+ \sum_{n=1}^{N}\sum_{m=1}^{M} \Re\Big\{ G\left(f, f_{n,l}(t), \sigma^2_{x,n,l,\mathrm{M}}\right)\, G^*\left(f, 0, \sigma^2_{x,m,\mathrm{F}}\right)\, \mu_{n,\mathrm{M}}(t)\, \mu^*_{m,\mathrm{F}} \Big\} \Bigg] \end{aligned} \tag{B.40}$$

channel has been analyzed over an observation interval T_{obs} of 4 s. The size of the room was 10 m long, 5 m wide, and 2.4 m high. The transmitter and the receiver had the same location at (5 m, 5 m, 2.25 m). The chosen number of fixed scatterers (walls and fixed objects) M was equal to 7. The number of moving scatterers N (moving persons) was chosen to be 1. In this scenario, we considered the head trajectory of the moving person. The path gains of the moving and fixed scatterers were computed using the following equations

$$c_{n,\text{M}} = \sigma_0 \sqrt{\frac{2\eta_N}{N}} \qquad \text{and} \qquad c_{m,\text{F}} = \sigma_0 \sqrt{\frac{2\eta_M}{M}} \tag{B.43}$$

respectively, where the parameters η_N and η_M allow for balancing the contribution of moving and fixed scatterers, respectively, which are subject to the following condition $\eta_N + \eta_M = 1$. The values of σ_0, η_N, and η_M were set to 1, 0.7, and 0.3, respectively. The chosen value for the window spread parameter σ_w is 0.033 s. The value of the parameter Δ introduced in Subsection B.3.2 was set to $2\sigma_w$. With reference to Fig. B.3, we consider a scenario that includes one moving scatterer representing the head of a moving person. There are three phases in the scenario:
Phase 1: The person walks 2 m at a constant speed in a time interval of 2.5 s.
Phase 2: When the person starts to fall forward, this phase lasts about 1 s until the head reaches the floor.
Phase 3: After the person's body reaches the floor, the moving scatterer becomes a fixed scatterer.
The head trajectory during the walking phase is modelled by

$$z(t) = h_{\text{step}} \cos\left(2\pi f_{\text{step}} t\right) + h_{\text{head}}. \tag{B.44}$$

The accuracy of this model has been confirmed in [20] by the trajectory extracted from a video surveillance-based human activity detection system. The azimuth angle of motion $\alpha_{v_n}(t)$ during the walking phase was 50°. The parameter h_{step} in (B.44) denotes the step height of the head during the walk. This parameter was equal to 2.7 cm. The parameter h_{head} stands for the height of the person, which was set to 1.7 m. The parameter f_{step} denotes the walking frequency, which is equivalent to the horizontal speed V_h over the step length L_s [21]. The value of the step length L_s was set to 30 cm. The horizontal speed value V_h during the walking phase was 0.8 m/s. The vertical speed V_v during the walking phase was computed by taking the derivative of (B.44) with respect to time. After the fall starts, V_h and V_v increase linearly with time until they reach the final speed values 2.5 m/s and 3.25 m/s at the end of fall, respectively [22].

Fig. B.4 depicts the results of the analysis of the spectrogram $S_\mu(f,t)$ by using (B.36). The simulation results were similar to the analytical results, but they were not included in this paper for brevity. In the simulation, the complex channel gain $\mu(t)$ was generated using the values provided earlier in this section. The values of $\theta_{n,\text{M}}$ and $\theta_{m,\text{F}}$ were obtained

from the outcomes of a random generator with uniform distribution between $(0, 2\pi]$. The simulation results have been obtained by simulating $\mu(t)$ in (B.27) by using MATLAB and then, computing the spectrogram from the simulated waveform $\mu(t)$. Fig. B.4 visualizes the influence of the head trajectory and walking speed on the spectrogram of the complex channel gain during the interval starting from $t = 0\,\mathrm{s}$ to $t = 2.5\,\mathrm{s}$. Also, this figure illustrates the impact of the variation of the head speed on the spectrogram during the fall starting from $t = 2.5\,\mathrm{s}$ to $t = 3.5\,\mathrm{s}$. During this interval, the speed increases rapidly with time due to the fall. From $t = 3.5\,\mathrm{s}$ until $t = 4\,\mathrm{s}$, the spectrogram has a strong spectral component at $f = 0\,\mathrm{Hz}$ because the head is no longer moving after the fall, i.e., its speed as well as the Doppler frequency are zero. It has to be mentioned that the characteristics of the approximated Doppler power spectrum of the fixed and moving scatterers is not obvious due to the impact of the cross-term reducing the resolution of the spectrogram. Fig. B.5 shows the auto-term of the spectrogram $S_{\mu}^{(a)}(f,t)$ according to (B.37). In this figure, it can be seen that the resolution of the spectrogram has been enhanced after removing the cross-term by taking the average of the spectrogram $S_{\mu}(f,t)$ over the random phases $\theta_{n,\mathrm{M}}$ and $\theta_{m,\mathrm{F}}$.

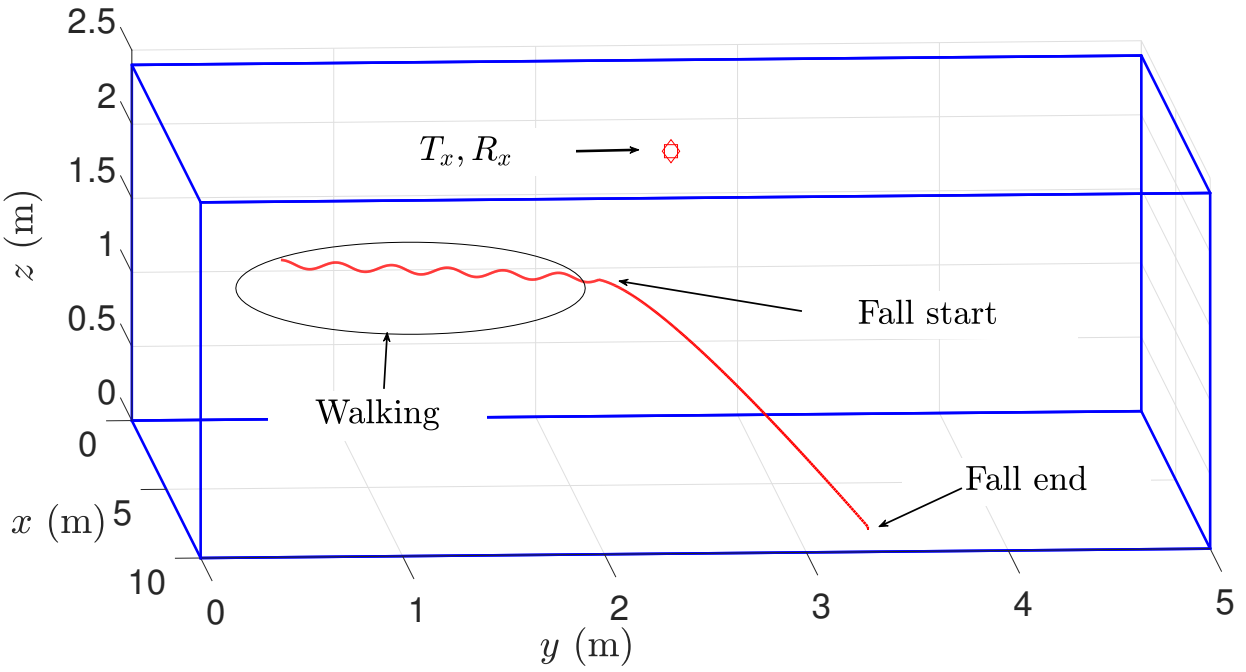

Figure B.3: Test scenario and the head trajectory.

Fig. B.6 depicts the TV mean Doppler shifts $B_f^{(1)}(t)$ and $B_{\mu}^{(1)}(t)$ obtained from (B.28) and (B.41), respectively. The TV mean Doppler shift $B_{\mu}^{(1)}(t)$ was computed numerically from the analytical expression in (B.41) and the simulation of the spectrogram using MATLAB. Although $B_{\mu}^{(1)}(t)$ is influenced by the cross-term of the spectrogram, one can recognize the impact of the fall during the interval between $t = 2.5\,\mathrm{s}$ and $t = 3.5\,\mathrm{s}$. There is a good

match between analytical and simulation results in Fig. B.6. Fig. B.7 depicts the TV Doppler spreads $B_f^{(2)}(t)$ and $B_\mu^{(2)}(t)$ obtained from (B.29) and (B.42), respectively. Again, the analytical solution of the spectrogram and the corresponding simulation results were used to obtain $B_\mu^{(2)}(t)$ by means of (B.42). Notice that, the impact of the fall on $B_\mu^{(2)}(t)$ is recognizable despite of the cross-term.

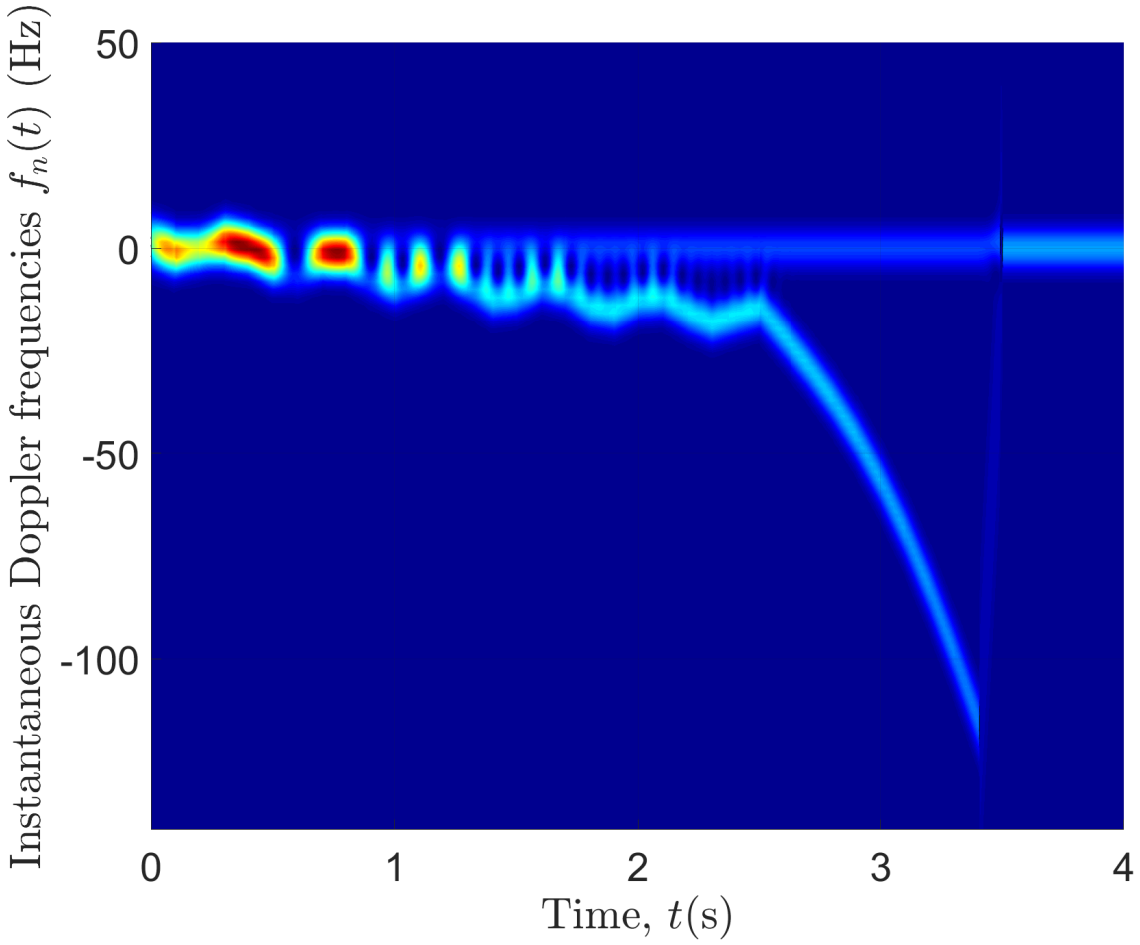

Figure B.4: Spectrogram (analysis) of the complex channel gain $\mu(t)$.

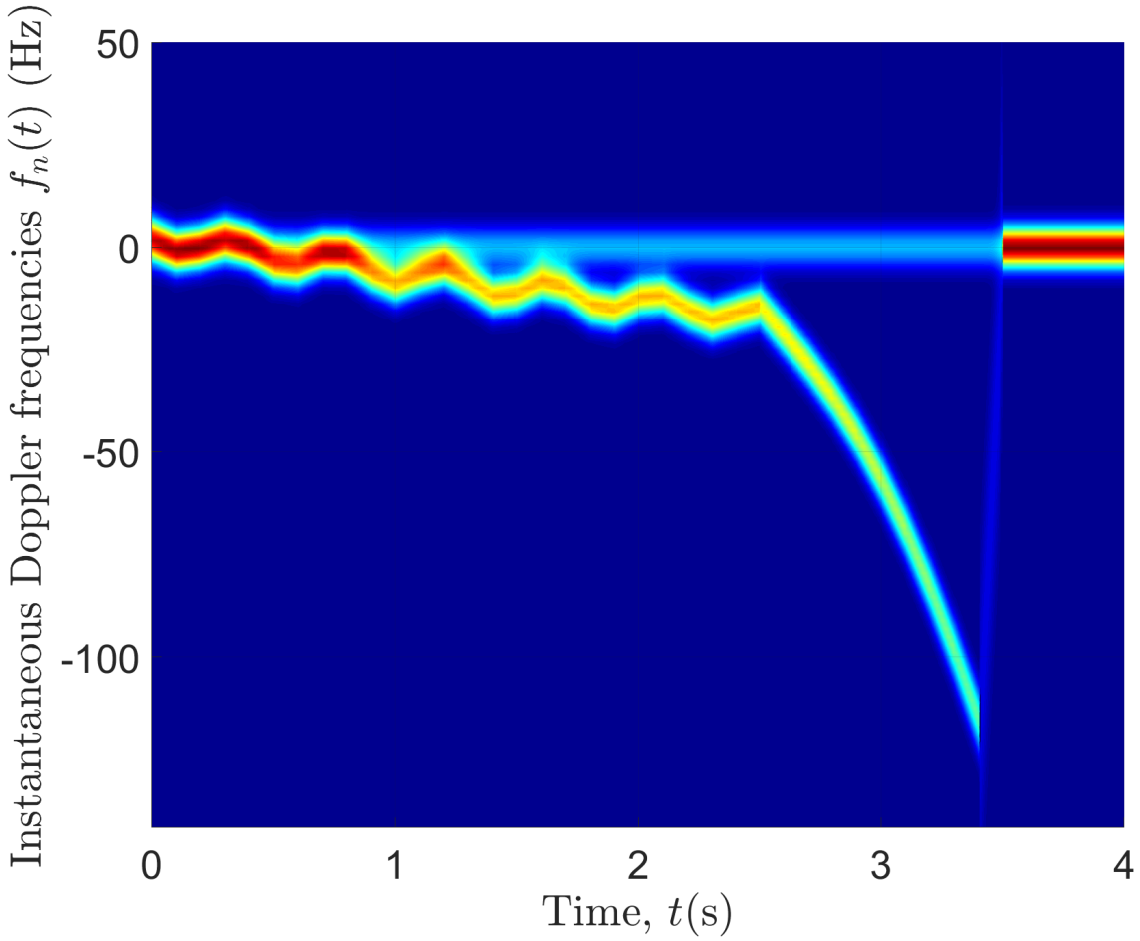

Figure B.5: The auto-term $S_{\mu}^{(a)}(f,t)$ (analysis) of the spectrogram of the complex channel gain $\mu(t)$.

B.6 Conclusion

In this paper, we presented a 3D multipath propagation model that reveals the influence of human activity on the characteristics of indoor multipath fading channels using the spectrogram. We started to model moving people as moving point scatterers. Then, we derived of the TV EAOAs, AAOAs, EAODs, AAODs, HAOMs, VAOMs, the Doppler frequencies caused by the moving point scatterers, and the complex channel gain of the indoor channels. After that, we showed the influence of moving people on such channels by providing an approximate solution of the spectrogram. Moreover, we showed the influence of the human activity on the TV mean Doppler shift and TV Doppler spread derived from the spectrogram. The spectrogram, TV mean Doppler shift, and TV Doppler spread enable us to distinguish between fall and walking activities. For future work, we plan to model people by a more

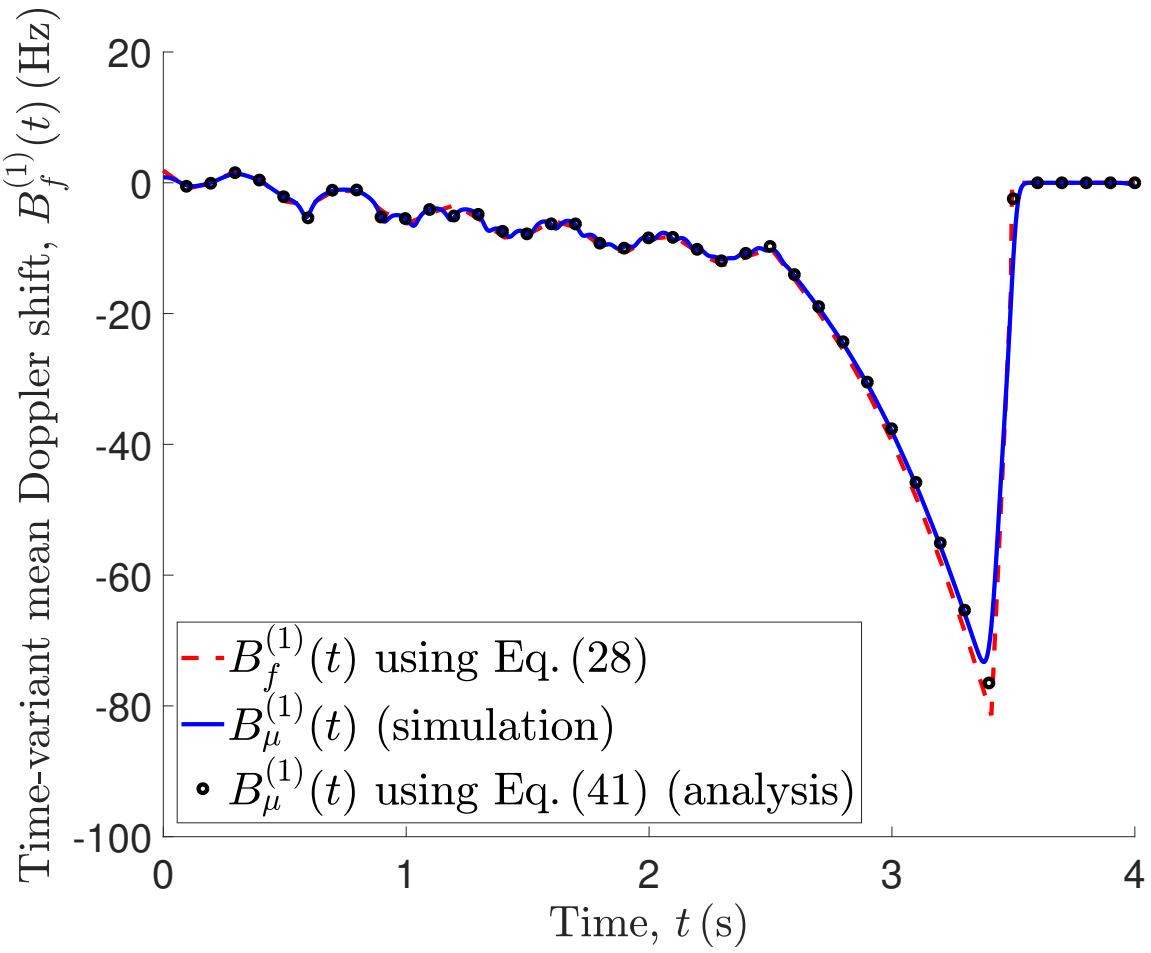

Figure B.6: TV mean Doppler shifts $B_f^{(1)}(t)$ and $B_\mu^{(1)}(t)$ obtained from (B.28) and (B.41), respectively.

realistic cluster of moving scatterers.

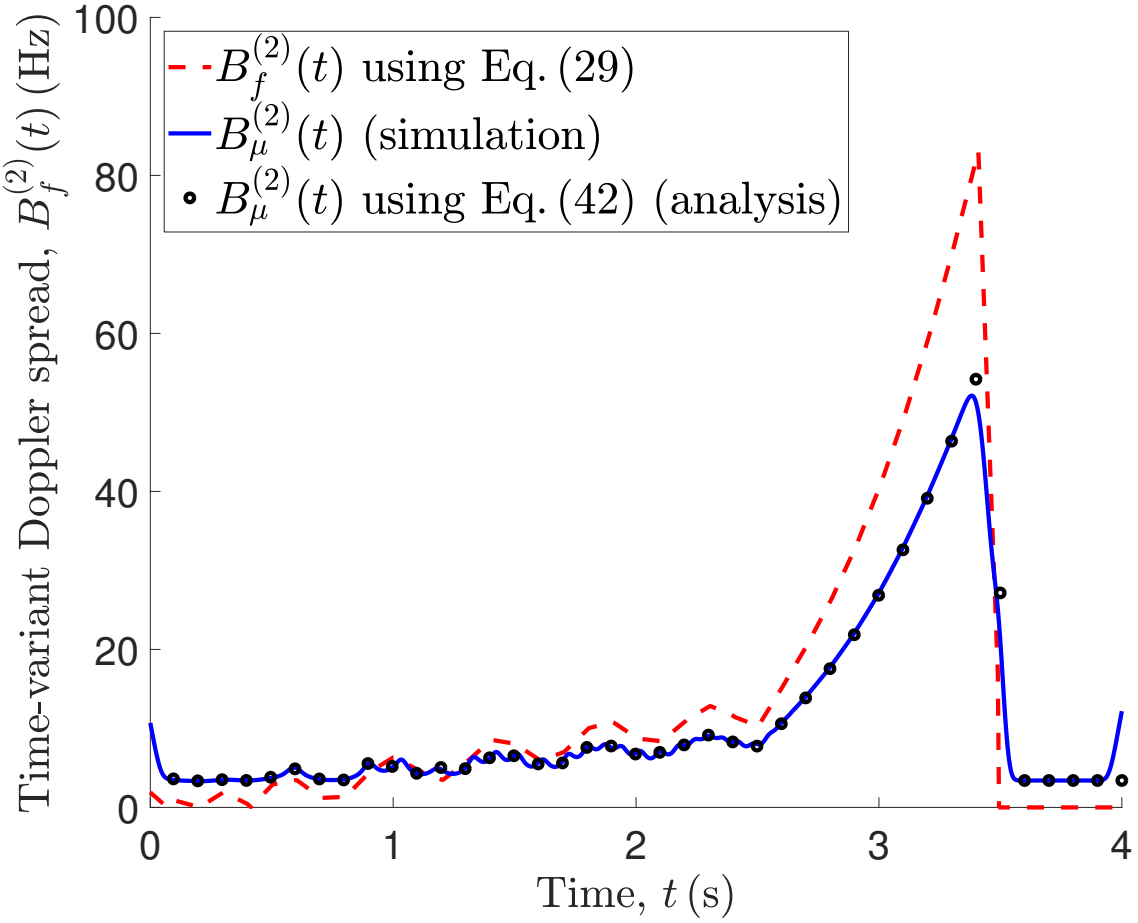

Figure B.7: TV Doppler spreads $B_f^{(2)}(t)$ and $B_\mu^{(2)}(t)$ computed according to (B.29) and (B.42), respectively.

Bibliography

[1] The European Commission, "The 2015 ageing report: underlying assumptions and projection methodologies," *European Economy*, Aug. 2014. DOI: 10.2765/76255.

[2] R. Cucchiara, A. Prati, and R. Vezzani, "A multi-camera vision system for fall detection and alarm generation," *Expert Systems*, vol. 24, no. 5, pp. 334–345, 2007. DOI:10.1111/j.1468-0394.2007.00438.x.

[3] C. Rougier, J. Meunier, A. St-Arnaud, and J. Rousseau, "3D head tracking for fall detection using a single calibrated camera," *Image Vision Computing.*, vol. 31, pp. 246–254, Mar. 2013.

[4] G. Anania *et al.*, "Development of a novel algorithm for human fall detection using wearable sensors," in *Proc. IEEE Sensors*, pp. 1336–1339, Oct. 2008.

[5] J. Wilson and N. Patwari, "See-through walls: Motion tracking using variance-based radio tomography networks," *IEEE Transactions on Mobile Computing*, vol. 10, pp. 612–621, May 2011.

[6] S. Sigg, M. Scholz, S. Shi, Y. Ji, and M. Beigl, "RF-sensing of activities from non-cooperative subjects in device-free recognition systems using ambient and local signals," *IEEE Transactions on Mobile Computing*, vol. 13, pp. 907–920, Apr. 2014.

[7] A. Zajić, "Modeling impact of moving scatterers on Doppler spectrum in wideband vehicle-to-vehicle channels," in *9th European Conference on Antennas and Propagation, EuCAP 2015*, pp. 1–5, May 2015.

[8] X. Zhao, Q. Han, X. Liang, B. Li, J. Dou, and W. Hong, "Doppler spectra for F2F radio channels with moving scatterers," *IEEE Trans. on Antennas and Propag.*, vol. 64, pp. 4107–4112, Sep. 2016.

[9] V. H. Pham, M. H. Taieb, J. Y. Chouinard, S. Roy, and H. T. Huynh, "On the double Doppler effect generated by scatterer motion," *REV Journal on Electronics and Communications*, vol. 1, pp. 30–37, Mar. 2011.

[10] A. Abdelgawwad and M. Pätzold, "On the influence of walking people on the Doppler spectral characteristics of indoor channels," in *Proc. 28th IEEE Int. Symp. on Personal, Indoor and Mobile Radio Communications, PIMRC 2017*, Montreal, Canada, Oct. 2017.

[11] F. Hlawatsch and G. F. Boudreaux-Bartels, "Linear and quadratic time-frequency signal representations," *IEEE Signal Processing Magazine*, vol. 9, pp. 21–67, Apr. 1992.

[12] J. B. Allen and L. R. Rabiner, "A unified approach to short-time Fourier analysis and synthesis," *Proceedings of the IEEE*, vol. 65, pp. 1558–1564, Nov. 1977.

[13] J. Allen, "Applications of the short-time Fourier transform to speech processing and spectral analysis," in *ICASSP '82. IEEE International Conference on Acoustics, Speech, and Signal Processing*, vol. 7, pp. 1012–1015, May 1982.

[14] L. G. Durand, J. Genest, and R. Guardo, "Modeling of the transfer function of the heart-thorax acoustic system in dogs," *IEEE Transactions on Biomedical Engineering*, vol. BME-32, pp. 592–601, Aug. 1985.

[15] J. Tribolet, "Applications of short-time homomorphic signal analysis to seismic wavelet estimation," *IEEE Transactions on Acoustics, Speech, and Signal Processing*, vol. 26, pp. 343–353, Aug. 1978.

[16] M. Pätzold and C. A. Gutiérrez, "Spectrogram analysis of multipath fading channels under variations of the mobile speed," in *Proc. 84rd IEEE Vehicular Technology Conference, IEEE VTC2016-Fall*, Montreal, Canada, Sept. 2016.

[17] M. Pätzold and C. A. Gutiérrez, "Enhancing the resolution of the spectrogram of non-stationary channels by using massive MIMO techniques," in *Proc. IEEE 86th Vehicular Technology Conference, VTC2017-Fall*, Toronto, Canada, Sep. 2017.

[18] M. Pätzold, C. A. Gutiérrez, and N. Youssef, "On the consistency of non-stationary multipath fading channels with respect to the average Doppler shift and the Doppler spread," in *Proc. IEEE Wireless Communications and Networking Conference, WCNC 2017*, San Francisco, CA, USA, Mar. 2017.

[19] B. Boashash, *Time-Frequency Signal Analysis and Processing – A Comprehensive Reference*. Elsevier, Academic Press, 2nd ed., 2015.

[20] S. U. Jung and M. S. Nixon, "Estimation of 3D head region using gait motion for surveillance video," in *4th International Conference on Imaging for Crime Detection and Prevention 2011, ICDP 2011*, pp. 1–6, London, UK, Nov. 2011. DOI: 10.1049/ic.2011.0105.

[21] T. Oberg, A. Karsznia, and K. Oberg, "Basic gait parameters: reference data for normal subjects, 10-–79 years of age," *Journal of Rehabilitation Research and Development*, vol. 33, no. 2, pp. 210–223, 1993.

[22] G. Wu, "Distinguishing fall activities from normal activities by velocity characteristics," *Journal of Biomechanics*, vol. 33, no. 11, pp. 1497 – 1500, 2000. DOI: https://doi.org/10.1016/S0021-9290(00)00117-2.